



1 **Precipitation and Microphysical Processes Observed by**
2 **Three Polarimetric X-Band Radars during HOPE**
3 **Xinxin Xie¹, Raquel Evaristo¹, Clemens Simmer¹, Jan Handwerker² and Silke**
4 **Trömel¹,**

5 ¹Meteorological Institute, University of Bonn, Bonn, Germany

6 ²Institute of Meteorology and Climate Research, Karlsruhe Institute of Technology,
7 Karlsruhe, Germany

8 *Correspondence to:* Xinxin Xie (xxie@uni-bonn.de)

9

10 **Abstract.** This study presents a first analysis of precipitation and related
11 microphysical processes observed by three polarimetric X-band Doppler radars
12 (BoXPol, JuXPol and KiXPol) in conjunction with a ground-based network of
13 disdrometers, rain gauges and vertically pointing micro rain radars (MRR) during the
14 High Definition Clouds and Precipitation for advancing Climate Prediction (HD(CP)²)
15 Observational Prototype Experiment (HOPE) during April and May 2013 in Germany.
16 While JuXPol and KiXPol were continuously observing the central HOPE area near
17 Forschungszentrum Juelich at a close distance, BoXPol observed the area from a
18 distance of about 48.5 km. MRRs were deployed in the central HOPE area and one
19 MRR close to BoXPol in Bonn, Germany. Seven disdrometers and three rain gauges
20 providing point precipitation observations were deployed at five locations within a 5
21 $\times 5$ km² region, while another three disdrometers were collocated with the MRR in
22 Bonn. The daily rainfall accumulation at each rain gauge/disdrometer location
23 estimated from the three X-band polarimetric radar observations showed a very good
24 agreement. Accompanying microphysical processes during the evolution of
25 precipitation systems were well captured by the polarimetric X-band radars and
26 corroborated by independent observations from the other ground-based instruments.



1 1. Introduction

2 In the frame of the project “High Definition Clouds and Precipitation for advancing
3 Climate Prediction” (HD(CP)²), which aims at improving the accuracy of climate
4 models in relation to cloud and precipitation processes, the HD(CP)² Observational
5 Prototype Experiment (HOPE) was conducted during April and May 2013 within the
6 study area of the Transregional Collaborative Research Center 32 (Simmer et al., 2015)
7 in the vicinity of the Juelich ObservatorY for Cloud Evolution (JOYCE) in Germany
8 (Löhnert et al., 2015). The HOPE was conducted in order to provide observations for
9 high-resolution climate models and to improve our understandings of cloud and
10 precipitation processes.

11 An array of ground-based instruments deployed during HOPE provided
12 comprehensive cloud and precipitation process observations. In this study we
13 concentrate on the precipitation monitoring instruments. Three polarimetric X-band
14 Doppler radars installed in Bonn (BoXPol) and in the vicinity of the JOYCE site
15 (JuXPol and KiXPol), respectively, were operated together to continuously monitor
16 3D precipitation patterns in order to obtain a holistic view of precipitating systems
17 from micro- and macro-physical perspectives. BoXPol and JuXPol were installed at a
18 distance of 48.5 km from each other and were operated by the Meteorological
19 Institute of the University of Bonn and the TERENO program of the Helmholtz
20 Association (<http://teodoor.icg.kfa-juelich.de>, Zacharias et al., 2011), respectively (see
21 Diederich et al., 2015a for details on both radars), while KiXPol, which was ~9.6 km
22 (~50.6 km) away from JuXPol (BoXPol), was deployed by the Karlsruhe Institute of
23 Technology (KIT). A network composed of rain gauges and disdrometers measured
24 local precipitation, and collocated Micro Rain Radars (MRR) simultaneously
25 measured vertical profiles of precipitation and raindrop size distributions (DSD).

26 Dual-polarization radars provide multiparameter measurements, which improve
27 quantitative precipitation estimation (QPE) compared to single polarization radars
28 (Zrníc and Ryzhkov, 1999; Zhang et al., 2001; Brandes et al., 2002; Ryzhkov et al.,



1 2014). A thorough comparison of retrieval algorithms for rainfall estimation using
2 polarimetric observables for the HOPE area can be found e.g. in Ryzhkov et al. (2014)
3 and Diederich et al. (2015b). Many studies has already shown the potential of
4 polarimetric radars to identify fingerprints of macro- and micro- physical processes
5 related to the evolution of precipitation systems (Kumjian and Ryzhkov, 2010, 2012;
6 Kumjian et al., 2012; Andric et al., 2013; Kumjian and Prat, 2014), based on the
7 sensitivities of polarimetric observables to particle size, shape, concentration and
8 composition (Bechini et al., 2013; Ryzhkov and Zrnica, 1998; Giangrande et al., 2008).
9 E.g., very few large rain drops near the ground or at the leading edge of a rain cell
10 result in a larger mean particle size and induce strong differential reflectivity (Z_{DR})
11 accompanied by small reflectivity (Z), which indicates the occurrence of size sorting
12 (Kumjian and Ryzhkov, 2012). Increasing mean particle sizes due to evaporation and
13 coalescence may enhance Z_{DR} , while Z is reduced during evaporation by the depletion
14 of small rain drops (Kumjian and Ryzhkov, 2010; Li and Srivastava, 2001). Z , Z_{DR}
15 and specific differential phase (K_{DP}) all decrease when large raindrops break up
16 (Kumjian and Prat, 2014). Such information thus can be used to validate cloud and
17 precipitation parameterization schemes.

18 The paper is structured as follows. Section 2 introduces the instrumentation deployed
19 during HOPE, while Section 3 presents the surface rainfall estimated from the radars,
20 in conjunction with disdrometers and rain gauges. Section 4 presents and discusses
21 the development of different precipitation systems and related microphysical
22 processes. Size sorting due to vertical wind shear and coalescence will be illustrated
23 via the combination of two X-band polarimetric radars. Another case of size sorting
24 captured by BoXPoL and a nearby MRR and disdrometers will also be examined in
25 detail. Finally, observed riming/aggregation signatures will be discussed. Conclusions
26 will be given in Section 5.

27

28 2. Instrumentation

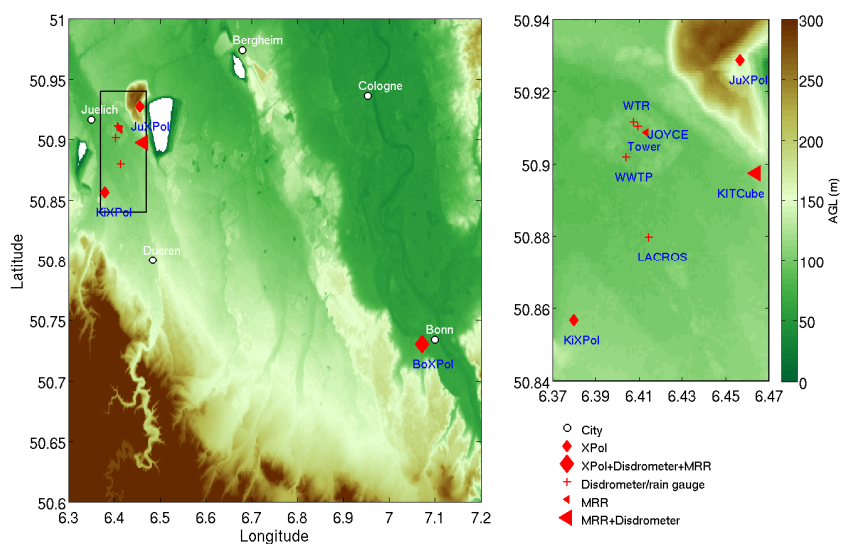


1 **2.1 Three X-band polarimetric radars**

2 The three polarimetric X-band Doppler radars BoXPol, JuXPol, and KiXPol were
3 operating at a frequency of 9.375 GHz. Topography and the locations of the radars,
4 disdrometers, rain gauges and MRRs are shown in Fig. 1. While JuXPol and KiXPol
5 were both performing observations in the vicinity of Juelich, Germany, BoXPol
6 observed the HOPE area from a distance of about 48.5 km on the roof of a building
7 next to the Meteorological Institute of the University of Bonn in Bonn, Germany,
8 collocated with one OTT Parsivel and two Thies optical laser disdrometers. The three
9 polarimetric radars provide the standard polarimetric variables observed in a
10 simultaneous transmit and receive (STAR) mode, namely Z , Z_{DR} , K_{DP} , and ρ_{HV}
11 (copolar correlation coefficient) in addition to the radial Doppler winds and its
12 variance. Detailed technical specifications of JuXPol and BoXPol can be found in
13 Diederich et al. (2015a) and for KiXPol under www.imk-tro.kit.edu/english/5438.php.
14 The calibration bias of the three radars were corrected following Diederich et al.
15 (2015a).

16 Figure 2 shows the operation duration of the three polarimetric radars during HOPE.
17 BoXPol had technical problems on 15 May 2013 and was back to work at around
18 0800UTC on 16 May 2013. JuXPol performed observation from 5 to 8 April 2013.
19 Afterwards, no measurements were available until 22 April 2013 due to technical
20 problems. From 26 to 29 April 2013, JuXPol was only taking range height indicators
21 (RHI) at 233.7° azimuth oriented towards JOYCE every minute. KiXPol started its
22 observations on 3 Apr 2013 but had two breakdowns during April. In May, when
23 KiXPol was performing only RHI scans on request, no PPIs were available.

24



1

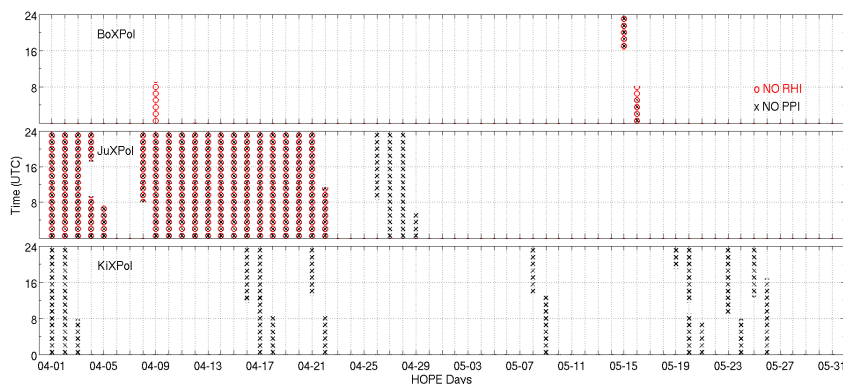
2 Figure 1. Location of the three polarimetric X-band radars (XPol) and associated
3 micro rain radars (MRR), rain gauges and disdrometers during HOPE. The right panel
4 is the zoomed-in region of the black box area on the left. The red diamond markers
5 indicate the locations of the X-band polarimetric radars, the red crosses indicate the
6 locations of disdrometers and/or rain gauges at the sites of LACROS (the Leipzig
7 Aerosol and Cloud Remote Observations System), KITCube (Kalthoff et al., 2013),
8 WWTP (wastewater treatment plant), Tower, WTR (wind-temperature-radar), and the
9 red triangles are the MRR locations at JOYCE and KITCube. White areas (elevations
10 below sea level) are open-pit mines.

11

12 The three polarimetric X-band radars were performing volume scans consisting of
13 stacked plan position indicators (PPI) with different scan strategies (Table 1). In
14 addition to the volume scans, BoXPol and JuXPol also performed RHIs and vertical
15 scans. A full volume scan of BoXPol and JuXPol takes about 5 min; in between RHI
16 scans and one vertical scan (bird bath scan) were performed. The two RHIs of
17 BoXPol were oriented towards JOYCE (290°) and LACROS (293.4°) after 9 April
18 2013, while JuXPol made RHIs only towards JOYCE. JuXPol made RHIs every



1 minute between 26 and 29 April 2013 followed by volume scans with PPIs at 10
2 elevations and one RHI and vertical scan in 5 minute intervals. KiXPoI performed
3 only volume scans at 14 elevations every 5 minutes from April 2013 on (see Table 1).
4 In May 2013, volume scans were interrupted on demand and instead RHI scans
5 directed towards the prevailing wind direction were performed with a temporal
6 resolution of 1 minute (Fig. 2).



7

8 Figure 2. Operation time of the polarimetric X-band radars BoXPoI, JuxPoI, and
9 KiXPoI during HOPE from 1 April to 31 May 2013, with the red circles indicating
10 “no range height indicator (RHI) available” and the black crosses indicating “no plan
11 position indicator (PPI) available”. KiXPoI performed only RHIs on demand in May
12 where “no PPI” was marked. The general scan strategies of the three polarimetric
13 X-band radars are described in Table 1.

14

15

16

17

18

19



1 Table 1 The three polarimetric radars during HOPE

	BoXPol	JuXPol	KiXPol
location in latitude/longitude	50.73°/7.07 °	50.93 °/6.46 °	50.86 °/6.38 °
elevation in m a.s.l.	100.0	310.0	116.6
PPIs at elevation in °	1/1.5/2.4/4.5/7/8.2/ 11/14/18/28	1/2/3.1/4.5/6/8.2/ 11/14/18/28	0.6/1.4/2.4/3.5/4.8 /6.3/8/9.9/12.2/14.8/ 17.9/21.3/25.4/30
RHIs at azimuth in °	309.5/298.6 (1-8 April); 290.0/293.4 (9 April-31 May)	118.6 (1-25 April); 233.7 (26 April-31 May)	on request in May
bird-bath scan	yes	yes	No
radial resolution in m	100 - 150	100 - 150	250
scan period	every 5 min	every 5 min	every 5 min

2

3 **2.2 Rain gauges, disdrometers, MRRs and radiosondes**

4 In the vicinity of JOYCE, disdrometers and rain gauges were installed within an area
 5 of approximately 25 km². Seven disdrometers observed surface rain rates and DSDs
 6 while three rain gauges measured rain accumulations (Table 2). The disdrometers and
 7 rain gauges close to Juelich are used to evaluate radar derived QPE. Disdrometer
 8 observations at BoXPol which is ~48.5 km away from JuXPol are not taken into
 9 account, considering the spatial and temporal variability of rainfall.

10 Three MRRs were deployed close to JOYCE, KITCube and BoXPol. At JOYCE and
 11 KITCube, the MRRs measured vertical DSD profiles with a vertical resolution of 100



1 m, at BoXPol 150 m. Due to the near field scattering effects, MRR observations at the
 2 first 3 gates are not used.

3 Radiosondes were launched regularly twice per day close to KITCube, one at 1100
 4 UTC and another at 2300 UTC. Additional radiosondes were launched during
 5 intensive observation periods (IOPs).

6 Table 2 Information on rain gauges and disdrometers deployed during HOPE

Site name	Location (Latitude, Longitude)	Instrument (quantity)	Temporal resolution (s)	operation period
KITCube	(50.90°,6.46°)	Joss-Waldvogel disdrometer (1)	60	1 Apr - 31 May 2013
		OTT Parsivel2 (1)	60	1 Apr - 31 May 2013
LACROS	(50.88°,6.41°)	OTT Parsivel2 (1)	30	2 May - 31 May 2013
WTR	(50.91°,6.41°)	OTT Parsivel2 (1)	30	17 Apr - 31 May 2013
		OTT Pluvio (1)	10	17 Apr - 31 May 2013
WWTP	(50.90°,6.40°)	OTT Parsivel2 (1)	30	17 Apr - 31 May 2013
		Tipping bucket rain gauge (1)	--	17 Apr - 31 May 2013
Tower	(50.91°,6.41°)	OTT Parsivel1 (1)	30	17 Apr - 31 May 2013
		OTT Parsivel2 (1)	30	17 Apr - 31 May 2013
		OTT Pluvio (1)	10	17 Apr - 31 May 2013
BoXPol	(50.73°,7.07°)	OTT Parsivel2 (1)	30	1 Apr - 31 May 2013
		Thies Disdrometer (2)	60	1 Apr - 31 May 2013
		OTT Pluvio (1)	60	1 Apr - 31 May 2013



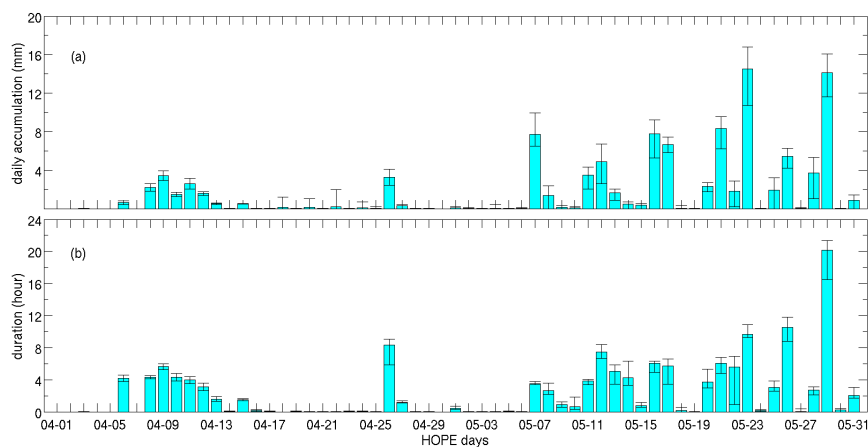
1 **3. Precipitation during HOPE**

2 We first compare QPE derived from the polarimetric radar observations with the
3 observations of the surface network of rain gauges and disdrometers, in order to
4 corroborate the consistency and accuracy of both estimates.

5 Figure 3 shows the daily rain accumulation and precipitation duration averaged over
6 the rain gauge/disdrometer observation sites in the HOPE region (Fig. 1). For rainfall
7 duration, only disdrometer observations are used since the weighing-type rain gauges
8 often indicate small noisy rain-like signals, which prevent accurate information on
9 rainfall duration. According to these observations, the maximum daily rain
10 accumulation was ~ 14.5 mm, the total rain accumulation during HOPE was ~ 104.8
11 mm, and the total rainfall time was ~ 144 hours, i.e., 10% of the total HOPE period.
12 The rainfall observations at the five locations are in good agreement with each other,
13 as indicated by the bars in Fig. 3, which show the full range of the observations.

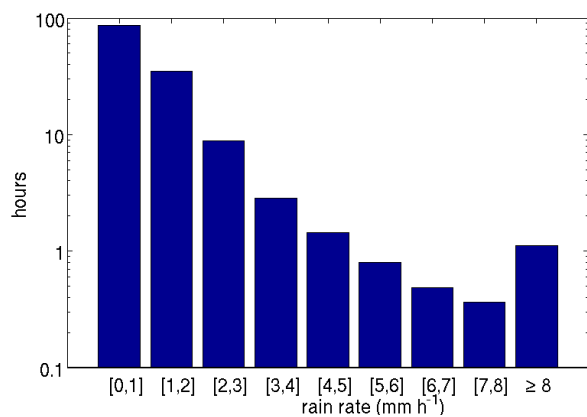
14 According to the disdrometer observations, precipitation during HOPE was not very
15 intense (Fig. 4). The distribution of rain intensities was calculated based on individual
16 measurements of disdrometers, instead of averaging over disdrometer sites at a single
17 time step. Rain rates determined at a temporal resolution of 1 minute were below less
18 than 2 mm h^{-1} for more than 88% of the total precipitation duration, while rain rates
19 above 5 mm h^{-1} were observed for less than 3 hours. Only one hour of rain rates above
20 8 mm h^{-1} did occur.

21



1

2 Figure 3. (a): Daily rainfall accumulation during HOPE. The height of the columns
3 indicates the mean value while the bars indicate the range of the maximum and
4 minimum rain accumulations observed by the 3 rain gauges and 7 disdrometers at the
5 five station locations (Fig. 1). (b): Daily precipitation duration derived only from the 7
6 disdrometers (see discussion in the text). Again the bars denote the range of the
7 observations.



8

9 Figure 4. Distribution of rain intensities observed over one minute by the
10 disdrometers in the inner HOPE area.

11



1 In accordance with the relatively light rainfall events during HOPE, the polarimetric
2 radar observables Z_{DR} and K_{DP} were low and quite noisy. Under these conditions,
3 most of the time, we simply used Marshall-Palmer relation for quantitative rainfall
4 estimations (Marshall and Palmer, 1948),

$$5 \quad Z_H = 200R^{1.5} \quad (\text{or } R = 0.029Z^{0.67}) \quad (1)$$

6 where Z_H (in $\text{mm}^6 \text{m}^{-3}$) is the radar reflectivity for horizontal polarization in linear
7 scale and R is the rain rate in mm h^{-1} .

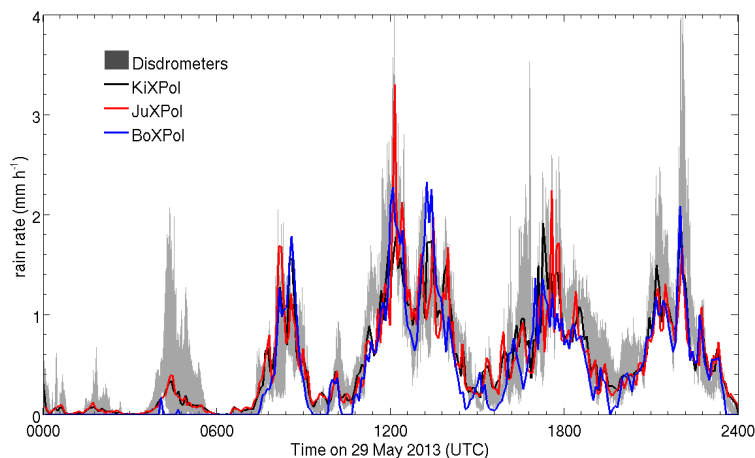
8 Since Equation (1) tends to overestimate stronger rain intensities (Zrnić et al., 2000;
9 Trömel et al., 2014b), the R- K_{DP} relation is employed for rain rate estimation when Z_H
10 is above 37 dBZ, i.e., the instantaneous rain rate is above 8 mm h^{-1} (Diederich et al.,
11 2015b; Ryzhkov et al., 2014). K_{DP} is independent of calibration and unaffected by
12 attenuation (Ryzhkov et al., 2014). Thus, following Diederich et al. (2015b) and
13 Ryzhkov et al. (2014), in this case the rain rate is determined by

$$14 \quad R = 16.9K_{DP}^{0.801} \quad \text{if } K_{DP} > 0 \quad (2)$$

15 where K_{DP} is the specific differential phase ($^{\circ} \text{ km}^{-1}$) and filtered from polarimetric
16 radar measurements following Hubbert and Bringi (1995).

17 Radar bins with copolar correlation coefficient $\rho_{HV} < 0.75$ have been neglected in
18 order to eliminate the ground clutter contamination. For JuXPol and KiXPol,
19 observations at elevations 4.5° and 3.5° , respectively, are used to calculate the rain
20 rates and avoid the possible impacts from a 120-m height meteorological tower at
21 Forschungszentrum Juelich, while an elevation of 1° is chosen for BoXPol rainfall
22 estimation since the radar beam at longer distance is less affected by the ground
23 clutter and certainly overshoots the meteorological tower. The mean beam diameter of
24 BoXPol over the HOPE area is around 850 m, which is almost 10 times larger than
25 that of JuXPol and KiXPol, and its beam height ($\sim 860 \text{ m}$) is about 2 times larger
26 comparing to JuXPol and KiXPol.

27

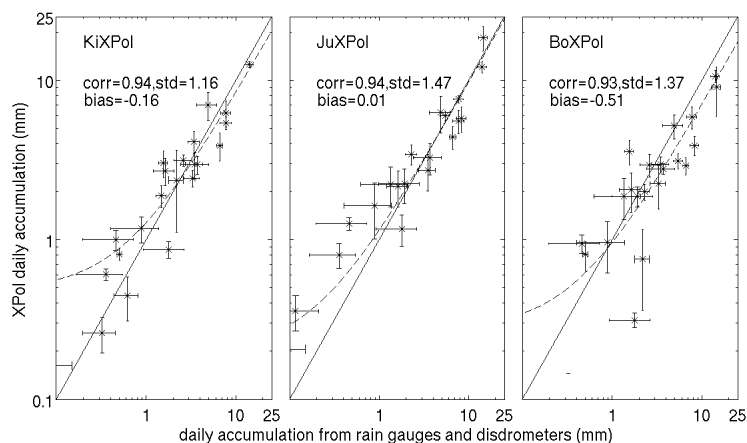


1

2 Figure 5. Time series of rain rates derived from observations of the seven
3 disdrometers and the three polarimetric radars on 29 May 2013. The shaded gray area
4 indicates the range of rain rates observed by the disdrometers with 1-min temporal
5 resolution in the HOPE area while the rain rate from the three polarimetric radar
6 observations is calculated at the radar gates that are coincident with disdrometer
7 locations and also averaged over the five disdrometer locations.

8

9 Figure 5 compares as an example the mean rain rates derived from the three X-band
10 polarimetric radar over the five disdrometer locations with the disdrometer
11 observations for 29 May 2013. Precipitation fell intermittently with five more intense
12 periods separated by short periods of no or very low rain rates and maximum rain
13 rates between 1 and 3 mm h⁻¹. In general, the variability of the radar-derived surface
14 precipitation matches very well the disdrometer measurements. JuXPol and KiXPol
15 are in a better agreement with the surface measurements than BoXPol for the very
16 lower rain rates, which probably suffers from the effects of non-uniform beam filling
17 effects due to the much larger distance from the HOPE area (Giangrande and Ryzhkov,
18 2008).

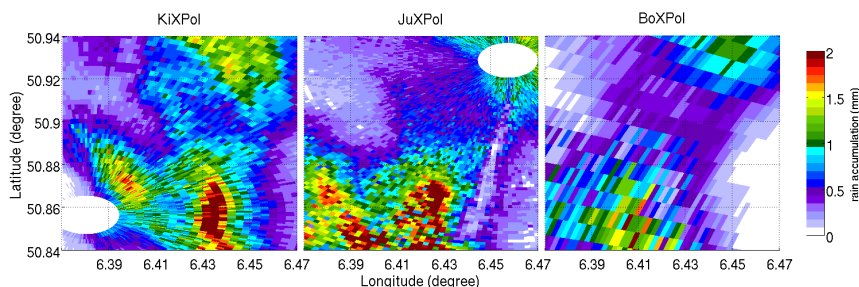


1

2 Figure 6. Mean daily radar-derived rain accumulation over the disdrometer/rain
3 gauge locations, compared to the surface precipitation observed by the rain gauges
4 and disdrometers in the HOPE area. The bars indicate the standard deviation of the
5 estimates from the particular radar (vertical bars) and from the surface observations
6 (horizontal bars) . The dashed black line is the best linear fit of the daily rain
7 accumulation on the logarithmic scale while the solid black line is the 1:1 line.

8

9 Daily-accumulated rainfall estimated by the three polarimetric radars are compared
10 with the observations of rain gauges and disdrometers in Fig. 6. Both estimates are
11 very consistent as indicated by correlations above 0.93. As for 29 May 2013, BoXPoL
12 estimates result in lower daily accumulations than for the other two radars, again
13 probably caused by beam broadening (Giangrande and Ryzhkov, 2008).



1

2 Figure 7. Rain accumulation over the HOPE area between 0830 and 0900 UTC (6
3 PPIs) on 29 May 2013 observed by the three polarimetric radars.

4

5 With a range resolution of 150/250 m and a beam diameter of approximately 87/850
6 m over the HOPE area, the three polarimetric radars allow to characterize the
7 precipitation patterns in the HOPE domain in high resolution, which will be important
8 for model evaluation. A 30-min rain accumulation over the inner HOPE area on 29
9 May 2013 shows that, the three radars estimates result in quite similar precipitation
10 patterns. Bins close to KiXPol and JuXPol were contaminated by ground clutters
11 while the beam broadening and height at the larger ranges deteriorates the similarity
12 between the BoXPol and KiXPol/JuXPol estimates (Fig. 7). A combination of the
13 three radar observations will definitely be an advantage to reconstruct the
14 precipitation patterns over the HOPE area. Since no adjustments of the $R-Z_H$ and
15 $R-K_{DP}$ relations were made, these results are very promising. The three radar
16 estimates together with the direct comparisons with the rain gauges and disdrometers
17 allow to attribute robust error estimates to these precipitation fields, which will be
18 very valuable when compared with model simulations.

19

20 4. Observed microphysical processes

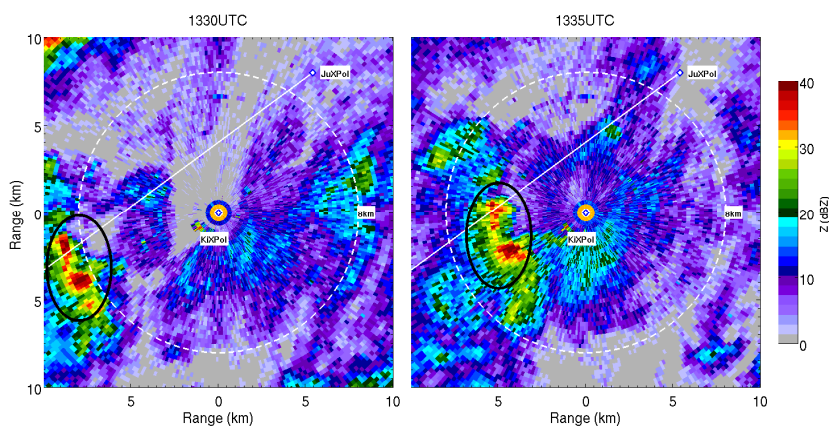
21 Falling hydrometeors are subject to growth and/or depletion by a range of
22 microphysical processes which leave their fingerprints in the spatial and temporal



1 evolution of several polarimetric moments. Since microphysical processes are
2 simulated in atmospheric models with increasing details, polarimetric radar
3 observations can be used for model validations and thus spur further improvements.
4 In this section we present three cases, where such microphysical processes could be
5 observed by the radars and substantiated by MRR and disdrometer observations.

6 **4.1 Case 1: Size sorting and coalescence**

7 On 26 Apr 2013, a cold front passed over Germany, which came with a large band of
8 stratiform rain that persisted from the morning hours until the end of the day. The
9 daily rain accumulation recorded by the surface observations was about 3.5 mm while
10 the precipitation lasted up to 8 hours (Fig. 3). Six radiosondes launched at KITCube at
11 0700 UTC, 0900 UTC, 1100 UTC, 1300UTC, 1600 UTC and 2300 UTC, respectively,
12 recorded a freezing level above 2100 m during daytime, which descended down to
13 830 m at about 2300 UTC.



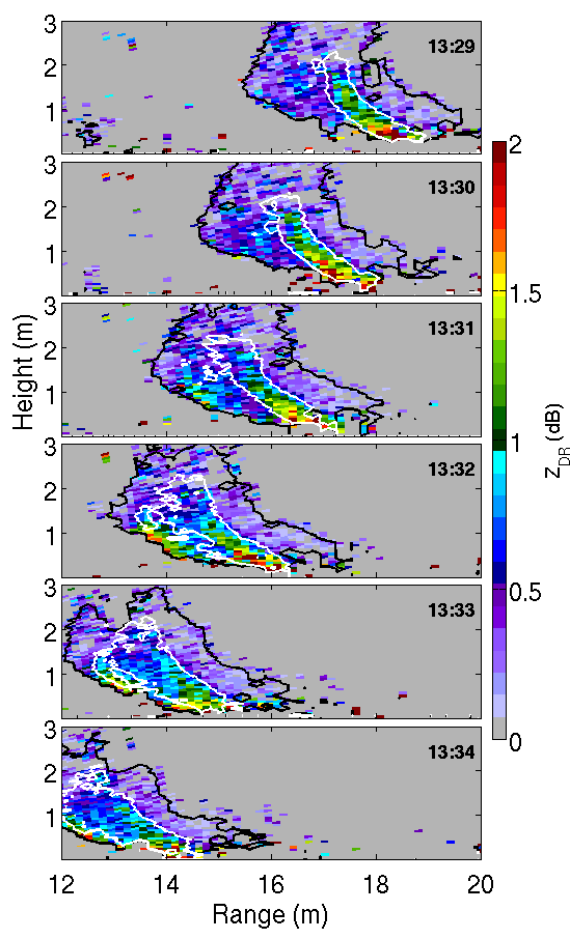
14

15 Figure 8. Reflectivity (Z_H) of KiXPol observed at an elevation angle of 3.5° at 1330
16 UTC and 1335 UTC on 26 April 2013. The precipitating cell examined in the text is
17 highlighted by the black ellipse. The white solid line indicates the azimuth direction
18 of the JuXPol RHIs, while the white dashed circle delineates the 8-km distance from
19 KiXPol.

20



- 1 KiXPol performed volume scans every 5 min on that day, with scan elevations
- 2 ranging from 0.6° to 30° (Table 1), while JuXPol made RHI scans in the direction of
- 3 JOYCE every minute.



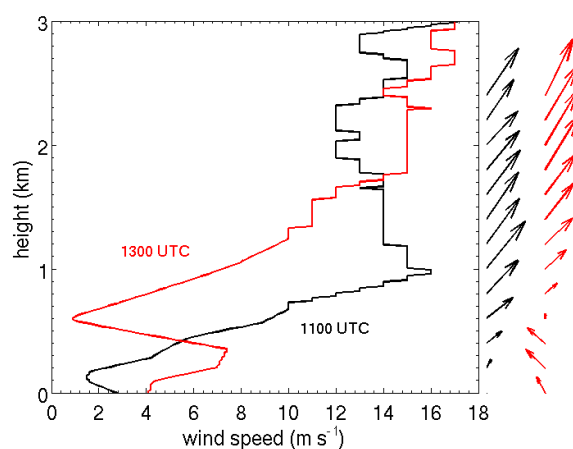
4
5 Figure 9. Sequence of RHIs of differential reflectivity (Z_{DR}) measured by JuXPol at
6 an azimuth angle of 233.7° between 1329 UTC and 1334 UTC on 26 April 2013
7 (from top to bottom). The contour lines indicate reflectivity values (Z_H) of 15 dBZ
8 (black) and 30 dBZ (white), respectively.

9



1 At 1330 UTC KiXPol observed a precipitating cell approaching the radar from the
2 southwest at about 10 km distance, which was moving towards JuXPol (Fig. 8). At
3 1335 UTC the cell was within 8 km from KiXPol, where it started to dissolve (not
4 shown). RHIs performed with JuXPol at the azimuth direction 233.7° nicely tracked
5 the approaching cell (Fig. 9).

6 The high temporal resolution of the JuXPol RHIs allows for a detailed insight into the
7 evolution of the precipitating cell. The cell was first observed by JuXPol at 1300 UTC
8 at about 45 km distance and kept moving towards JuXPol with low reflectivities at
9 about 20 dB (not shown). At 1329 UTC, JuXPol detected the precipitating cell
10 entering its RHI at 20 km range (Fig. 9). In the center of the precipitating cell tilted
11 towards the northeast by the wind shear (See Fig. 10), near surface Z_{DR} values were
12 up to 2 dB while Z_H was above 30 dBz. Z_{DR} increases towards the ground concurrent
13 with an increasing Z_H . This behavior is a clear sign of coalescence, which shifts small
14 raindrops to larger sizes and increases the mean raindrop size (Kumjian and Prat,
15 2014).



16
17 Figure 10 Wind profiles derived from radiosondes launched at KITCube at 1100 UTC
18 and 1300 UTC. The arrows on the right indicate the wind vector (0° indicates the
19 north) while their lengths are proportional to wind speed.



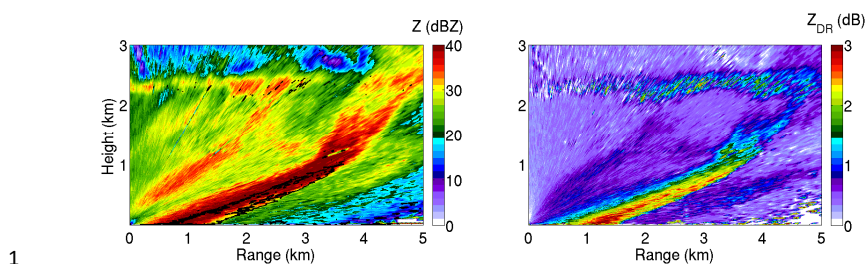
1 While moving towards JuXPol, the tilt of the cell led to a concentration of large rain
2 drops at the leading edge of the precipitating cell, where their larger fall speed
3 separates them from the smaller droplets which largely remain in the flow volume
4 (e.g., Kumjian and Ryzhkov (2012)). From 1329 UTC to 1330 UTC, Z_{DR} at the
5 leading edge of the cell is below 0.5 dB (Fig. 9). At 1331 UTC, Z_{DR} begins increasing
6 and later on reaches up to 2 dB while Z_H remains in the order of 15 dBz in that region.
7 When the cell begins to dissipate as it moves forward, Z_{DR} decreases down to ~ 1 dB
8 both in the center and upstream of the precipitating cell.

9 **4.2 Case 2: Size sorting due to vertical wind shear**

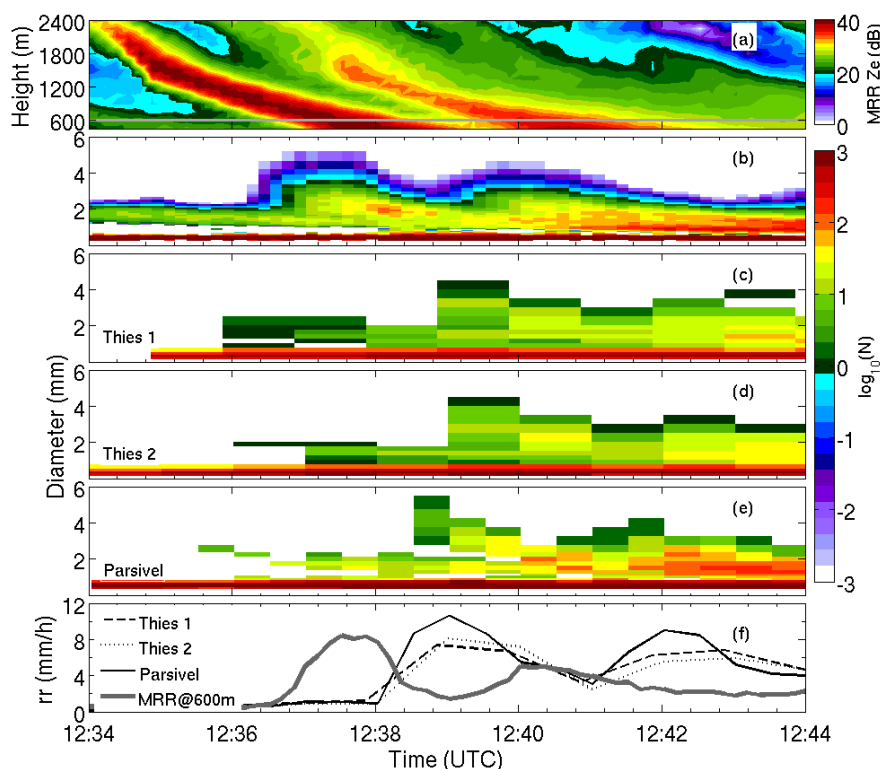
10 A second case on size sorting caused by the vertical wind shear was well captured by
11 BoXPol on 17 May 2013. A deep low pressure system reaching from the surface up to
12 200 hPa was found over the Northeast Atlantic and the British Isles on the previous
13 day, while a surface low was moving from the western Mediterranean to the north,
14 towards central Europe. As a result a complex pattern of fronts was affecting France
15 and Germany due to the interaction of both systems. On 17 May 2013, a stationary
16 front along with a through of warm air aloft passed over West Germany, moving
17 eastwards. Low atmosphere levels were characterized by high humidity and a sharp
18 West-East temperature gradient. A band of mostly stratiform rain affected
19 south-western and western Germany earlier in the day, while later on convective rain
20 with lightning activity developed over south east and central Germany. About 8 mm
21 of rain accumulated over 6 hour time spans as recorded by the disdrometers (Fig. 3).

22

23



1
2 Figure 11. Reflectivity (Z_H , left) and differential reflectivity (Z_{DR} , right) observed by
3 BoXPOL at an azimuth angle of 290° at 1240 UTC on 17 May 2013. The black isoline
4 in the left panel indicates the 2-dB Z_{DR} contour line.
5 The melting layer can be easily identified by the enhanced Z_H and Z_{DR} at an altitude
6 of ~ 2.2 km in the BoXPOL RHI performed at an azimuth angle of 290° (Fig. 11).
7 Similar to the first case presented above, the strong Z_{DR} at the leading edge indicates
8 the increase of mean raindrop size due to the accumulation of large raindrops by size
9 sorting.



1

2 Figure 12. Different instrument observations located within distances of 5 meters
3 close (200 m) to the BoXPoI location in Bonn, Germany, between 1234 UTC and
4 1244 UTC on 17 May 2013. (a): Reflectivity observed by vertically pointing micro
5 rain radar (MRR). The grey horizontal solid line indicates the 600 m height level. (b):
6 MRR-observed DSDs at 600 m altitude. (c) DSDs observed by a Thies disdrometer
7 with its transmitter and receiver line pointing along the east-west direction (Thies 1);
8 (d) same as (c) but for a Thies disdrometer pointing along the south-north direction
9 (Thies 2); (e) Same as (c) except for an OTT Parsivel disdrometer; (f) Rain rate
10 observed by an MRR at 600 m height and the three disdrometers collocated with the
11 MRR at the BoXPoI station.

12



1 At 200 m distance from BoXPol, vertical profiles of DSDs were observed by an MRR.
2 Figure 12 shows the time series of MRR-derived reflectivity (Panel a) with the
3 corresponding DSDs at an altitude of 600 m (Panel b). The first cell of a precipitation
4 system passed BoXPol and the MRR before 1240 UTC with reflectivities up to 40
5 dBz in the center, followed by a second peak with reflectivities up to 35 dBz (Fig.
6 12a). The derived DSDs indicate that, fast falling large raindrops tend to concentrate
7 at the upstream side of the cell, while raindrops less than 3 mm in diameter have a
8 larger number concentration downstream (Fig. 12b).

9 The OTT Parsivel and Thies optical laser disdrometers collocated with the MRR also
10 captured the precipitation event on that day (Fig. 12c-12f). One Thies disdrometer
11 was deployed with its transmitter-receiver line in the west-east direction (Thies 1) and
12 the other in the south-north direction (Thies 2). For the surface DSDs shown in Fig.
13 12b-12e, the largest raindrops collected by the two Thies disdrometers are below 4
14 mm after 1239 UTC. Similar to MRR observations, however, the Parsivel observed
15 larger raindrops up to 5 mm at an earlier time step since it was operated at a temporal
16 resolution of 30 s. It implies that a temporal resolution of better than 1 min is required
17 to better interpret the DSD evolution caused by size sorting due to vertical wind shear
18 and to improve the surface rainfall estimations.

19 The surface rain rates observed by the three disdrometers differ from the MRR
20 observations at 600 m considering the spatial and temporal shifts (approximately 2
21 min) (Fig. 12f). The maximum rain rate estimated from the MRR at 600 m is ~ 8 mm
22 h^{-1} at 1238 UTC, with a second peak of ~ 6 mm h^{-1} at 1240 UTC. While the Parsivel
23 overestimates the rain rates, comparing to the MRR observations, the two Thies
24 disdrometers tend to slightly underestimate the rain rates with their rough time
25 resolution (1 min). Nevertheless, these observations are consistent with the occurrence
26 of the size sorting process shown from the radar observations..

27 **4.3 Case 3: Riming/aggregation processes observed by JuXPol**

28 On 29 May 2013 a cut-off process was underway over western and middle Europe,



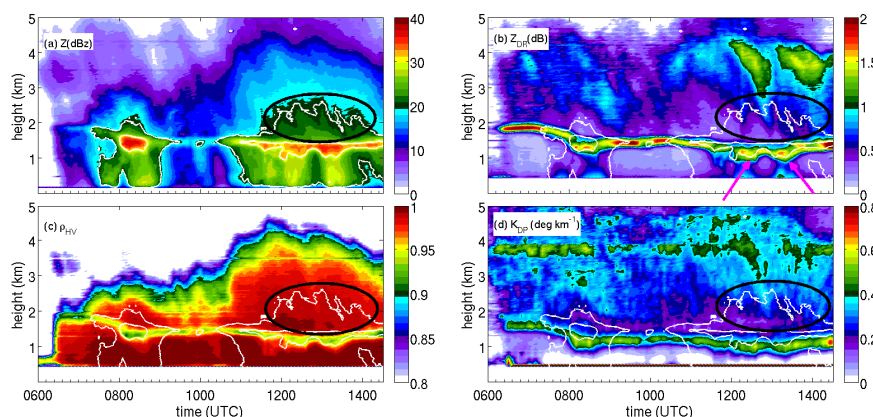
1 resulting in a broad and well defined upper level vortex. At lower levels the pressure
2 distribution was more complex with several small surface lows and generally weak
3 pressure gradients. One of these surface lows, initially situated over southern England
4 at 0000 UTC, moved to eastern France during the day. The corresponding cold front
5 became quasi-stationary, as indicated by a sharp θ_e (equivalent potential temperature)
6 gradient over Be-Ne-Lux and western Germany (not shown). At 0000 UTC and 0600
7 UTC frontogenetic forcing was strongest due to deformational processes in the
8 vicinity of the front as it interacted with a second low over the northern half over
9 Germany. This resulted in a subsequent reinforcement of frontal precipitation over the
10 HOPE area until 1200 UTC. During and after that intensification period the frontal
11 temperature gradient gradually dissolved due to evaporative cooling and the advection
12 of a colder maritime air mass also on the warm side of the front. As a consequence
13 frontal precipitation weakened by the end of the day.

14 The daily rain accumulation for 29 May 2013 recorded by the surface observations
15 was ~ 14 mm while precipitation lasted up to 20 hours (Fig. 3): this was the day with
16 the longest rainy period which also lead to the second largest daily rain accumulation
17 during HOPE. Three radiosondes were launched at the location of KITCube, one at
18 2300 UTC on 28 May and two at 1100 UTC and 2300 UTC on 29 May. According to
19 the soundings, the freezing level was located at ~ 2.2 km at 2300 UTC on 28 May
20 2013 and subsided down to ~ 1.7 km at 1100 UTC on 29 May 2013.

21 Figure 13 shows so-called Quasi-Vertical Profiles (QVPs) of Z_H , Z_{DR} , ρ_{HV} and K_{DP}
22 based on JuXPol measurements at 18° elevation angle between 0600 and 1430 UTC.
23 QVPs were first used by Trömel et al. (2014a) to reliably estimate backscatter
24 differential phase δ and Ryzhkov et al. (2016) further expanded the QVP methodology
25 and demonstrated its multiple benefits. The QVPs of polarimetric variables are
26 obtained by azimuthal averaging of the radar data collected during conical PPI scans
27 at higher antenna elevation angles in order to reduce statistical errors of the variables
28 and assign their average vertical profiles to a conical volume in a time-height display.
29 QVPs are especially beneficial for monitoring the temporal evolution of



1 microphysical processes active on a larger scale.



2

3 Figure 13. (a) Time series of Quasi-Vertical Profiles (QVPs) of Z_H derived from
4 PPIs measured with JuXPOL at 18° elevation on 29 May 2013 between 0600UTC and
5 1430UTC. The white lines indicate the 20 and 30 dBZ contours of Z_H ; (b), (c) and (d):
6 the same time series as (a) but for Z_{DR} , ρ_{HV} and K_{DP} , respectively. The black ellipses
7 highlight the area for aggregation/riming while the magenta arrows in Panel (b)
8 indicate the Z_{DR} saggings (see text for detail).

9

10 The most striking feature in Fig. 13 is the descent of the melting layer from 1.8 km
11 down to ~ 1.5 km height between 0700 and 0900 UTC. After 1200 UTC, a region
12 enhanced K_{DP} above 3.5 km accompanied with $Z_{DR} > 1.2$ dB aloft can be identified.
13 Bands of enhanced Z_{DR} and bands of enhanced K_{DP} are both considered as signatures
14 of dendritic growth (Kennedy and Rutledge, 2011). According to the radiosonde
15 ascending at 1100 UTC, the temperature zone of $-10^\circ\text{C} \sim -15^\circ\text{C}$ which favors the
16 growth of ice dendrites is located between 3.8 and 4.7 km. Thus, we may suspect
17 dendrites growing above 3.5 km especially after 1200 UTC (Fig. 13).

18 When following the height evolution of polarimetric variable structures above the
19 melting layer (ML) after 1200 UTC (Fig. 13), riming/aggregation processes are
20 indicated by enhancements of Z_H and ρ_{HV} above the ML while Z_{DR} and K_{DP} decrease
21 with height in unison above the ML after 1200 UTC (ellipses in Fig. 13). Z_{DR} and K_{DP}



1 depressions aloft associated with increases in Z_H and ρ_{HV} above the ML suggest
2 increases of ice particle mean sizes due to riming and/or aggregation. Recently,
3 Moisseev et al. (2015) argued that the processes responsible for enhanced K_{DP} - and
4 Z_{DR} -bands might be different: they advocated that the K_{DP} bands are caused by high
5 number concentrations of oblate relatively dense ice particles (early aggregates) and
6 are linked to the onset of aggregation processes, while Z_{DR} bands in the absence of
7 K_{DP} bands are observed when crystal growth is the dominating snow growth
8 mechanism and the number concentration is lower. Following their arguments, it can
9 also be speculated that aggregation processes are ongoing near the end of the
10 observation period shown in Fig. 13.

11 Discrimination between riming and aggregation is important for aviation security,
12 since riming implies the existence of supercooled liquid water above the freezing
13 level, which could result in dangerous icing on aircrafts. Riming is also associated
14 with embedded updrafts, convective development and thus precipitation enhancement.
15 In the presence of such updrafts, enhanced condensation of water vapor occurs and
16 leads to small liquid droplets which may be accreted by dry snowflakes. These rimed
17 snowflakes may grow fast and reach large sizes with higher terminal velocity before
18 they fall through the ML. Due to their enhanced terminal velocity, they melt at a
19 lower height and lead to the “sagging” signature of the bright band in terms of Z_{DR}
20 and ρ_{HV} (Ryzhkov et al., 2016).

21 In Fig. 13, reduced Z_{DR} combined with enhanced Z_H and ρ_{HV} above the ML occurs at
22 times, and also “sagging” signatures are clearly visible at around 1200 UTC and 1300
23 UTC (the magenta arrows in Fig. 13b). Starting from the bottom of the Z_{DR} - and K_{DP} -
24 bands at about 3 km height at 1200 UTC, Z_{DR} decreases and Z increases downwards
25 most probably due to aggregation and/or riming. Here Z_{DR} reduces down to a few
26 tenths of a dB just above the level where melting starts. However, this reduction is
27 expected to be more intense for riming than for aggregation. Riming makes the ice
28 particles more spherical leading to a lower Z_{DR} by 0.1 – 0.3 dB (Ryzhkov et al., 2016).
29 Thus, we speculate that riming causes the “sagging” effects of Z_{DR} and ρ_{HV} combined



1 with relatively low Z_{DR} above the ML around 1200 UTC and 1300 UTC. To more
2 reliably distinguish between riming and aggregation, we require additional
3 measurements indicative e.g. of associated updrafts and supercooled liquid water
4 above ML, which could be provided by additional microwave radiometers and cloud
5 radars.

6 The discussed examples have clearly shown how polarimetric radars can be used to
7 identify and distinguish between different microphysical processes, like warm rain
8 processes and ice particle formation and growth. Converting the output of NWP
9 models into polarimetric radar variables and using a polarimetric forward radar
10 operator would provide an opportunity to validate the representation of the discussed
11 microphysical processes in such models.

12

13 **5. Conclusions**

14 This study presents a summary of rainfall observations and some examples of related
15 microphysical processes occurring during HOPE between 1 April and 31 May 2013.
16 At that time three X-band polarimetric Doppler radars observing the central HOPE
17 area of about $5 \text{ km} \times 5 \text{ km}$ over which a surface network of rain gauges, disdrometers
18 and MRRs was deployed to assess the accuracy of the radar-based precipitation
19 observations and to demonstrate the capability of polarimetric radars to detect
20 microphysical processes. Rainfall accumulations at the daily and even hourly scale
21 were surprisingly consistent between the different observations demonstrating the
22 high quality of QPE based on R-Z and R- K_{DP} relations at least for the low intensity
23 rainfall events prevalent during HOPE.

24 The combined observations of polarimetric radars and collocated instruments
25 demonstrated the ability of radar polarimetry to detect several microphysical
26 processes by so-called polarimetric fingerprints during the development and evolution
27 of precipitation systems. These fingerprints clearly identify microphysical processes
28 like coalescence, size sorting and riming/aggregation. Size sorting by wind shear was



1 e.g. well captured by the JuXPoI and BoXPoI RHI scans and corroborated by the
2 collocated MRR and disdrometer observations. While there were clear signs of other
3 processes like riming and aggregation, their distinction requires additional analysis in
4 conjunction with other independent observations e.g. from microwave radiometers,
5 lidars and cloud radars deployed at the JOYCE site, which is the focus of an ongoing
6 study.

7

8 **Acknowledgements**

9 This research was funded by the Federal Ministry of Education and Research in
10 Germany (BMBF) through the research programme “High Definition Clouds and
11 Precipitation for Climate Prediction - HD(CP)²” (FKZ: 01LK1219A and 01LK1210A).
12 We thank Martin Lennefer and Kai Muehlbauer at University of Bonn and the
13 SFB/TR 32 (Transregional Collaborative Research Center 32, <http://www.tr32.de/>)
14 funded by the German Research Foundation (DFG) for maintaining the instruments
15 and make the radar data available. We thank Patric Seifert from the Leibniz Institute
16 for Tropospheric Research (TROPOS) for providing the OTT Parsivel data at the
17 LACROS station. We also acknowledge Norbert Kalthoff and his colleagues from
18 the Karlsruhe Institute of Technology (KIT) for providing the observation data at
19 KITCube station and KiXPoI observations during HOPE.

20

21 **References**

- 22 Andric, J., Kumjian, M. R., Zrnica, D. S., Straka, J. M., and Melnikov, V. M.:
23 Polarimetric signature above the melting layer in winter storms: An observational
24 and modeling study, *J. Appl. Meteor. Climatol.*, 52, 682-700, 2013.
- 25 Bechini, R., Baldini, L., and Chandrasekar, V.: Polarimetric Radar Observations in the
26 Ice Region of Precipitating Clouds at C-Band and X-Band Radar Frequencies, *J.*
27 *Appl. Meteor. Climatol.*, 52, 1147-1169, 10.1175/jamc-d-12-055.1, 2013.
- 28 Brandes, E. A., Zhang, G., and Vivekanandan, J.: Experiments in Rainfall Estimation



- 1 with a Polarimetric Radar in a Subtropical Environment, *J. Appl. Meteor.*, 41,
2 674-685, 2002.
- 3 Diederich, M., Ryzhkov, A., Simmer, C., Zhang, P., and Trömel, S.: Use of Specific
4 Attenuation for Rainfall Measurement at X-Band Radar Wavelengths. Part I:
5 Radar Calibration and Partial Beam Blockage Estimation, *J. Hydrometeorol.*, 16,
6 487-502, 10.1175/jhm-d-14-0066.1, 2015a.
- 7 Diederich, M., Ryzhkov, A., Simmer, C., Zhang, P., and Trömel, S.: Use of Specific
8 Attenuation for Rainfall Measurement at X-Band Radar Wavelengths. Part II:
9 Rainfall Estimates and Comparison with Rain Gauges, *J. Hydrometeorol.*, 16,
10 503-516, 10.1175/jhm-d-14-0067.1, 2015b.
- 11 Giangrande, S. E., Krause, J. M., and Ryzhkov, A. V.: Automatic Designation of the
12 Melting Layer with a Polarimetric Prototype of the WSR-88D Radar, *J. Appl.
13 Meteor. Climatol.*, 47, 1354-1364, 10.1175/2007jamc1634.1, 2008.
- 14 Giangrande, S. E., and Ryzhkov, A. V.: Estimation of Rainfall Based on the Results of
15 Polarimetric Echo Classification, *J. Appl. Meteor. Climatol.*, 47, 2445-2462,
16 10.1175/2008jamc1753.1, 2008.
- 17 Hubbert, J., and Bringi, V. N.: An Iterative Filtering Technique for the Analysis of
18 Copolar Differential Phase and Dual-Frequency Radar Measurements, *J. Atmos.
19 Oceanic Technol.*, 12, 643-648,
20 10.1175/1520-0426(1995)012<0643:aifft>2.0.co;2, 1995.
- 21 Kalthoff, N., Adler, B., Wieser, A., Kohler, M., Träumner, K., Handwerker, J.,
22 Corsmeier, U., Khodayar, S., Lambert, D., Kopmann, A., Kunka, N., Dick, G.,
23 Ramatschi, M., Wickert, J., and Kottmeier, C.: KITcube – a mobile observation
24 platform for convection studies deployed during HyMeX, *Meteor. Z.*, 22,
25 633-647, 10.1127/0941-2948/2013/0542, 2013.
- 26 Kennedy, P. C., and Rutledge, S. A.: S-Band Dual-Polarization Radar Observations of
27 Winter Storms, *J. Appl. Meteor. Climatol.*, 50, 844-858, 10.1175/2010jamc2558.1,
28 2011.
- 29 Kumjian, M. R., and Ryzhkov, A. V.: The Impact of Evaporation on Polarimetric



- 1 Characteristics of Rain: Theoretical Model and Practical Implications, *J. Appl.*
2 *Meteor. Climatol.*, 49, 1247-1267, 10.1175/2010JAMC2243.1, 2010.
- 3 Kumjian, M. R., Ganson, S. M., and Ryzhkov, A. V.: Freezing of Raindrops in Deep
4 Convective Updrafts: A Microphysical and Polarimetric Model, *J. Atmos. Sci.*, 69,
5 3471-3490, 10.1175/JAS-D-12-067.1, 2012.
- 6 Kumjian, M. R., and Ryzhkov, A. V.: The Impact of Size Sorting on the Polarimetric
7 Radar Variables, *J. Atmos. Sci.*, 69, 2042-2060, 10.1175/JAS-D-11-0125.1, 2012.
- 8 Kumjian, M. R., and Prat, O. P.: The Impact of Raindrop Collisional Processes on the
9 Polarimetric Radar Variables, *J. Atmos. Sci.*, 71, 3052-3067,
10 10.1175/JAS-D-13-0357.1, 2014.
- 11 Löhnert, U., Schween, J. H., Acquistapace, C., Ebell, K., Maahn, M., Barrera-Verdejo,
12 M., Hirsikko, A., Bohn, B., Knaps, A., O'Connor, E., Simmer, C., Wahner, A.,
13 and Crewell, S.: JOYCE: Jülich Observatory for Cloud Evolution, *B. Amer.*
14 *Meteor. Soc.*, 96, 1157-1174, 10.1175/bams-d-14-00105.1, 2015.
- 15 Li, X., and Srivastava, R. C.: An Analytical Solution for Raindrop Evaporation and Its
16 Application to Radar Rainfall Measurements, *J. Appl. Meteorol.*, 40, 1607-1616,
17 2001.
- 18 Marshall, J. S., and Palmer, W. M. K.: The Distribution of Raindrops with Size, *J.*
19 *Meteorol.*, 5, 165-166, 10.1175/1520-0469(1948)005<0165:tdorws>2.0.co;2,
20 1948.
- 21 Moisseev, D. N., S. Lautaportti, J. Tyynela, and S. Lim: Dual-polarization radar
22 signatures in snowstorms: role of snowflake aggregation, *J. Geophys. Res.*,
23 10.1002/2015JD023884.
- 24 Ryzhkov, A., Diederich, M., Zhang, P., and Simmer, C.: Potential Utilization of
25 Specific Attenuation for Rainfall Estimation, Mitigation of Partial Beam
26 Blockage, and Radar Networking, *J. Atmos. Oceanic Technol.*, 31, 599-619,
27 10.1175/jtech-d-13-00038.1, 2014.
- 28 Ryzhkov, A., Zhang, P., Reeves, H., Kumjian, M., Tschallener, T., Simmer, C. and
29 Trömel, S.: Quasi-vertical profiles - a new way to look at polarimetric radar data,



- 1 Accepted for publication in J. Atmos. Oceanic Technol., 2016.
- 2 Ryzhkov, A. V., and Zrníc, D. S.: Discrimination between Rain and Snow with a
3 Polarimetric Radar, J. Appl. Meteorol, 37, 1228-1240,
4 10.1175/1520-0450(1998)037<1228:dbrasw>2.0.co;2, 1998.
- 5 Simmer, C., Masbou, M., Thiele-Eich, I., Amelung, W., Bogena, H., Crewell, S.,
6 Diekkrüger, B., Ewert, F., Franssen, H.-J. H., Huisman, J. A., Kemna, A.,
7 Klitzsch, N., Kollet, S., Langensiepen, M., Löhnert, U., Mostaqimur Rahman, A.,
8 S. M., Rascher, U., Schneider, K., Schween, J., Shao, Y., Shrestha, P., Stiebler,
9 M., Sulis, M., Vanderborght, J., Vereecken, H., van der Kruk, J., Waldhoff, G.,
10 and Zerenner, T.: Monitoring and Modeling the Terrestrial System from Pores to
11 Catchments – the Transregional Collaborative Research Center on Patterns in the
12 Soil-Vegetation-Atmosphere System, B. Amer. Meteor. Soc., 96, 1765–1786,
13 10.1175/bams-d-13-00134.1, 2015.
- 14 Trömel, S., Ryzhkov, A. V., Zhang, P., and Simmer, C.: Investigations of Backscatter
15 Differential Phase in the Melting Layer, J. Appl. Meteorol. Climatol., 53,
16 2344-2359, 10.1175/jamc-d-14-0050.1, 2014a.
- 17 Trömel, S., Ziegert, M., Ryzhkov, A. V., Chwala, C., and Simmer, C.: Using
18 Microwave Backhaul Links to Optimize the Performance of Algorithms for
19 Rainfall Estimation and Attenuation Correction, J. Atmos. Oceanic Technol, 31,
20 1748-1760, 10.1175/jtech-d-14-00016.1, 2014b.
- 21 Zacharias, S., Bogena, H., Samaniego, L., Maude, M., Fuss, R., Putz, T., Frenzel, M.,
22 Schwank, M., Baessler, C., Butterbach-Bahl, K., Bens, O., Borg, E., Brauer, A.,
23 Dietrich, P., Hajnsek, I., Helle, G., Kiese, R., Kunstmann, H., Klotz, S., Munch, J.,
24 C., Papen, H., Priesack, E., Schmid, H.P., Steinbrecher, R., Rosenbaum, U.,
25 Teutsch, G., Vereecken, H.: A Network of Terrestrial Environmental
26 Observatories in Germany. Vadose Zone J., 10, 955-973, 10.2136/vzj2010.0139,
27 2011.
- 28 Zhang, G., Vivekanandan, J., and Brandes, E.: A method for estimating rain rate and
29 drop size distribution from polarimetric radar measurements, IEEE Trans. Geosci.



- 1 Remote Sens., 39, 830-841, 10.1109/36.917906, 2001.
- 2 Zrnić, D. S., and Ryzhkov, A. V.: Polarimetry for Weather Surveillance Radars, B.
- 3 Amer. Meteor Soc, 80, 389-406,
- 4 10.1175/1520-0477(1999)080<0389:pfwsr>2.0.co;2, 1999.
- 5 Zrnić, D. S., Keenan, T. D., Carey, L. D., and May, P.: Sensitivity Analysis of
- 6 Polarimetric Variables at a 5-cm Wavelength in Rain, J. Appl. Meteorol., 39,
- 7 1514-1526, 10.1175/1520-0450(2000)039<1514:saopva>2.0.co;2, 2000.
- 8